



Published in final edited form as:

IEEE Trans Biomed Eng. 2020 December ; 67(12): 3307–3316. doi:10.1109/TBME.2020.2983443.

A Multi-Dimensional Analysis of a Novel Approach for Wireless Stimulation

Parinaz Abiri [Student Member, IEEE],

Department of Bioengineering and Department of Medicine, University of California, Los Angeles, Los Angeles, CA 90095, USA

Alireza Yousefi [Student Member, IEEE],

Department of Electrical Engineering, University of California, Los Angeles, Los Angeles, CA 90095, USA

Arash Abiri,

Department of Medicine, University of California, Los Angeles, Los Angeles, CA 90095, USA

Varun Gudapati,

Department of Medicine, University of California, Los Angeles, Los Angeles, CA 90095, USA

Yichen Ding,

Department of Medicine, University of California, Los Angeles, Los Angeles, CA 90095, USA

Kim-Lien Nguyen,

Department of Medicine, University of California, Los Angeles, Los Angeles, CA 90095, USA

Ahmad Abiri,

Department of Medicine, University of California, Los Angeles, Los Angeles, CA 90095, USA

Dejan Markovic [Member, IEEE],

Department of Electrical Engineering, University of California, Los Angeles, Los Angeles, CA 90095, USA

Yu-Chong Tai [Member, IEEE],

Department of Medical Engineering, California Institute of Technology, Pasadena, CA 91125, USA

Tzung K. Hsiai*

Department of Bioengineering and Department of Medicine, University of California, Los Angeles, Los Angeles, CA 90095, USA.

Abstract

The elimination of integrated batteries in biomedical implants holds great promise for improving health outcomes in patients with implantable devices. However, despite extensive research in wireless power transfer, achieving efficient power transfer and effective operational range have remained a hindering challenge within anatomical constraints. *Objective:* We hereby demonstrate an intravascular wireless and batteryless microscale stimulator, designed for (1) low power

*(correspondence thsiai@mednet.ucla.edu).

dissipation via intermittent transmission and (2) reduced fixation mechanical burden via deployment to the anterior cardiac vein (ACV, ~3.8 mm in diameter). *Methods:* We introduced a unique coil design circumferentially confined to a 3 mm diameter hollow-cylinder that was driven by a novel transmitter-based control architecture with improved power efficiency. *Results:* We examined wireless capacity using heterogenous bovine tissue, demonstrating >5 V stimulation threshold with up to 20 mm transmitter-receiver displacement and 20° of misalignment. Feasibility for human use was validated using Finite Element Method (FEM) simulation of the cardiac cycle, guided by pacer phantom-integrated Magnetic Resonance Images (MRI). *Conclusion:* This system design thus enabled sufficient wireless power transfer in the face of extensive stimulator miniaturization. *Significance:* Our successful feasibility studies demonstrated the capacity for minimally invasive deployment and low-risk fixation.

Keywords

wireless medical devices; wireless pacemaker; inductive power transfer; implantable medical devices; implantable cardiovascular devices

I. INTRODUCTION

IMPLANTABLE stimulators, including cardiac pacemakers and neuromodulation devices used for spinal cord, deep brain, and peripheral nerve stimulation, demand the use of device leads for the transmission of power from the pulse generator to the stimulation electrodes. Despite their extensive use, implanted leads can result in a variety of medical complications. In cardiac pacemakers alone, which account for over 1 million annual implants, nearly one-in-ten patients experience lead-associated complications [1], [2]. This is compounded by immune-mediated responses that render lead extraction life-threatening in case of complications [3]. Despite recent advances in implantable biomedical devices, the utilization of wireless power transfer is still absent as a means to replace device wires. This is due to anatomical constraints that limit sufficient power delivery. This work will focus on the application of wireless power transfer for stimulation of the heart, which presents the combined challenges of space limitations and rhythmic motion.

Recent years have introduced battery-based leadless pacemakers to mitigate lead-based complications [4]. However, integrating a battery within the pacer body increases the device size and weight [4]–[6]. The device's consequently large deployment catheter limits anatomic accessibility and increases radiation exposure during implantation [5], [6]. Fixation anchors of leadless pacers also experience repetitive myocardial contractile forces, predisposing the device to detachment and embolization in addition to increasing the risk for right ventricular (RV) perforation and pericardial effusion [5], [6]. Furthermore, in response to battery exhaustion or device malfunction, immune-mediated tissue adhesion and local fibrosis further render device extraction challenging [5], [6].

As an alternative approach to power implantable devices, harvesting cardiac and lung motion or ultrasonic vibration has been proposed to address battery limitations [7]–[15]. While an appealing technology, these solutions have yet to demonstrate practical use due to their reliance on an endocardial anchor or invasive epicardial fixation as a result of device size,

their dependency on multiple implants and incisions, or their inability to harvest sufficient energy for pacing [7]–[15].

Wireless power transfer via electromagnetic induction (nearfield) has also been established as a means to achieving a leadless system, but with a compromise in device size while aiming to maintain power transfer efficiency and meeting Specific Absorption Rate (SAR) limits [16]–[24]. A large device prevents implant feasibility within anatomical confines, and exceeding SAR limits results in life-threatening tissue heating and damage. Inductive power transfer for miniature stimulators in various applications have also been proposed, but with insufficient power capacity for long-term cardiac pacing while meeting transmitter size requirements [25]–[30]. Far-field wireless pacers have also yet to demonstrate the capacity to meet power demands [31], [32] or independently control pulse rate, duration, and voltage threshold [33].

To address the aforementioned complications and constraints, we demonstrated an inductively-powered, batteryless, intravascular pacer combined with a unique intermittent transmission control architecture. Our validation studies were performed in alignment with standard market-released peak pacing amplitudes (5 V [6]) and average patient pacing thresholds (0.8 V [34]). We examined wireless capacity using heterogenous bovine tissue, demonstrating > 5 V output voltage with an electrode impedance of 1000 ohms (Ω) at a displacement up to 20 mm and misalignment up to 20°. Pacing threshold remained above the mean amplitude of 0.80 V in response to various combinations of displacement (up to 30) mm and misalignment (up to ~45°). Feasibility analyses of wireless capacity indicated sufficient power transfer over MRI-guided anatomical displacements and angular variations with adequate safety margin to tolerate variations. These analyses were demonstrated at 23-fold below the SAR limits, thus establishing a large safety margins for both power level regulation and absorption limits. Overall, this work demonstrated the fundamental basis for an efficient wirelessly powered stimulation system with sufficient operational range for cardiac pacing with translational implications in alternative organ stimulations.

II. MATERIALS & METHODS

A. Control System Design

We designed an inductive power transfer system in which the pacer pulse activity was entirely controlled by intermittent power input into the wireless power transmitter tank circuit. As such, the corresponding wireless receiver contained no internal control structure or charge storage unit (e.g. battery) with its function being solely to transfer its input power to the stimulating electrodes.

Through this mechanism, the pacer would enter “idle mode” during the non-stimulation period and switch to “active mode” during stimulation. For all studies, we set the “active mode” length to 1 ms. This stimulation duration is considered to be in the upper range for an effective pulse width as a result of the leveling effect of the strength-duration curve [35]. At 60 beats per minutes (BPM), this 1 ms “active mode” would be separated by intervals of 999 ms in “idle mode.” Unlike continuous wireless power transmission, the receiver would not consume power during the prominent “idle mode” as there would be no power-consuming

circuitry or function in the remote receiver during this period; this would effectively reduce the power consumption by 1000-fold.

This reduction would be further amplified by a shorter pulse duration within a given time period. Thus, the power efficiency is often improved by > 1000-fold as pulse duration typically ranges between 0.2 ms to 1 ms.

B. Coil Design

The design of an inductive power transfer system is guided by the optimization of power transfer efficiency (PTE) as defined by Equation 1 [36]:

$$\eta = \frac{k^2 Q_1 Q_{2L}}{1 + k^2 Q_1 Q_{2L}} \cdot \frac{Q_{2L}}{Q_L} \quad (1),$$

Where k is the coupling coefficient, Q_1 is the quality factor of the transmitter coil, Q_2 is the quality factor of the receiver coil, $Q_{2L} = Q_2 Q_L / (Q_2 + Q_L)$, and $Q_L = R_{Load} / 2\pi f L_2$.

Thus, we may increase PTE by optimizing Q and k . The coupling coefficient is primarily defined by the geometry of the coils and their relative positions, with distance and alignment both impacting coupling strength [37]:

$$k = \frac{r_1^2 r_2^2}{\sqrt{r_1 r_2} (\sqrt{r_1^2 + D^2})^3} \cos(\theta) \quad (2),$$

Where r_1 is the radius of the transmitter, r_2 is the radius of the receiver, D is the distance between the transmitter and receiver, and θ is the misalignment angle.

The Equality factor is similarly impacted by geometry due to its dependence on inductance, with additional guiding variables as show in Equation 3 [38]:

$$Q = \frac{2\pi f L}{R} \quad (3),$$

where f is the operating frequency, L is antenna inductance, and R is the effective ohmic losses.

In a system experiencing alternating current (AC), resistance is defined by the complex relationship developed as a result of the skin effect, as shown in Equations (4) and (5) [38], and proximity effect, which is impacted by the spacing between adjacent turns of a coil [39]:

$$R_{AC} = \frac{l}{2\pi a \sigma \delta} \quad (4),$$

where l is wire length, a is wire radius, σ is wire conductivity, and δ is skin depth defined by Equation (5) [38].

$$\delta = \frac{1}{\sqrt{\pi f \mu_o \mu_r \sigma}} \quad (5),$$

where μ_o is the permeability of air, and μ_r is the permeability of copper.

In the case of biomedical implants, the coils must be designed within a space-limited environment with potential for variations in distance and misalignment. Optimization of PTE is thus guided by the environmental constraints. While both the coupling coefficient and quality factor appear to have minimal capacity for manipulation due to their primary reliance on geometric variables (as shown in Eq. (2) and (3)), and thus implant position, modifications to the standard looped coil design can introduce a potential mechanism for a more efficient inductive link.

Thus, we aimed to demonstrate wireless cardiac pacing via intravascular fixation by utilizing a novel receiver coil structure. We designed the receiver coil (Fig. 1A in yellow) based on the limitations of the Anterior Cardiac Vein (ACV), where the pacer would be implanted on the heart. Thus, it was configured to 2.8 mm in diameter and 15 mm in length with a hollow center to allow for passage of blood. We fabricated the coil with 5 elliptical turns of a 30 AWG polyurethane-insulated wire with spacing in between each turn such that the planar coil measured 7 mm (width) \times 9 mm (length). The spacing was implemented to minimize proximity effect losses. This planar elliptical coil was then continued as a meandering tail with spacing between each turn such that the tail measured 2.8 mm (width) \times 6 mm (length). The elliptical segment of the coil was then folded into a 3-dimensional half-cylindrical coil with the planar meandering tail. The curved design allowed for increased surface area of field capture while remaining within the confines of the vascular implant position.

We fabricated the transmitter coil (Fig. 1A in blue) as a planar coil to minimize device thickness for subcutaneous implantation with minimal aesthetic impact on the patient. We used current pacemaker pulse generator size to guide length and width at 40 mm \times 40 mm. Thus, we fabricated the transmitter coil with 18 circular turns of a 23 AWG wire with an inner diameter of 10 mm and outer diameter of 40 mm. Due to the impact of the proximity effect on coil resistance, the wires were spaced apart at a distance equivalent to that of the wire diameter.

Upon design of the coils, the tank circuit (Fig. 1A) was completed using Equation 6 [38]:

$$C_{res} = \frac{1}{L(2\pi f)^2} \quad (6),$$

Where C_{res} is the tank capacitance, L is coil inductance, f is the operating frequency.

The properties of the inductive link are shown in Table I. The transmitter tank circuit was supplied through a Class E Power Amplifier for optimal efficiency [40]–[42] and the receiver tank circuit drained into a voltage doubler for AC-DC conversion prior to tissue stimulation via platinum-deposited electrodes.

Implant locations for the transmitter and receiver (Fig. 1B) were based on three criteria: (1) minimal distance between the communicating components, (2) ease of deployment, (3) minimal impact by complications such as stenosis of the selected vessel. For the transmitter, this was selected as subcutaneously in the anterior chest, with the aim of similar implant technique within a surgical pocket as existing pacemaker pulse generators. For the receiver, this was selected as the anterior cardiac vein (ACV) [43] with aim of catheter-based delivery through the coronary sinus and distal to the greater cardiac vein.

C. Measurement of Wireless Power Transfer Range

To determine the range of function for the proposed pacer, we placed the transmitter and receiver at varying distances apart and with different degrees of misalignment. The average distance between the two implant positions (subcutaneous for the transmitter and inside the ACV for the receiver) was set to 20 mm [44]. We thus examined wireless power transfer capacity at distances of 10 mm to 30 mm between the transmitter and receiver. Due to myocardial contractility, the angle between the two components also varies over the cardiac cycle. Thus, we measured up to 45° misalignment in four directions: (1) horizontal x-axis misalignment, (2) horizontal y-axis misalignment, (3) vertical x-axis misalignment, and (4) vertical y-axis misalignment.

All of the measurements were performed with a segment of bovine tissue that included bone, muscle, adipose, and connective tissue, placed between the transmitter and receiver (Fig. 2). We compensated for the change in distance between the components via the addition or removal of layers of bovine muscle tissue. The electrode-tissue interface impedance was simulated with a $1000\ \Omega$ resistor, which is the impedance of a typical high-impedance pacemaker stimulation lead electrode [45]. We then measured the voltage across the load in the receiver given an instantaneous input power of 1.26 W to the transmitter.

D. Simulating Pacing Function Across a Cardiac Cycle

We analyzed 4-dimensional (3-dimensions + time) coronal magnetic resonance images (MRIs) of the thorax through a cardiac cycle to determine the relative motion between the implanted transmitter and receiver components. The transmitter, to be implanted subcutaneously anterior to the ribs and sternum, was simulated as an immobile object. The receiver position was simulated by inserting a phantom object in the MRI slices at the location of the ACV (Fig. 3A). We adjusted the size of the phantom to the nearest voxel size relative to the actual device size, resulting in a rectangular phantom object of size $4.14 \times 3.60 \times 21.31$ mm.

Next, we created four versions of the 3-D phantom image, each containing a red marking in one of the four corners on the larger surface (4.14×21.31 mm) of the phantom. These markers served as representative landmarks of the surface of the phantom that would have the greatest contact with the epicardium. As previously described [46], deformable image registration (DIR) was applied on each time point of the 4-D thoracic MRI to generate 3-D displacement fields that represented the instantaneous cardiac motion at discrete time points in the cardiac cycle. To simulate the moving phantom at any given time point, the 3-D phantom image of the previous time point was transformed using the 3-D displacement field

that was calculated for the given time point. Thus, a 4-D phantom image was generated for each marked version of the original 3-D phantom to simulate its motion throughout the cardiac cycle.

To spatially track the landmarks over time, we first extracted the red color spectrum from each marked 4-D phantom image. In each 3-D image of each 4-D phantom image, we determined the 3-D location of the landmark by calculating the weighted average of non-zero pixel, using the pixel intensities as the weights. The resulting output was four 3-D points in each time point representing four corners of the phantom in a single averaged slice (Fig. 3B).

Next, we computed the centroid of the four points in each time point to trace the changing 3-D position of the phantom relative to the initial position. We also calculated for the normal vector to the four points in each time point to trace the changing angular alignment of the phantom relative to the initial time point.

We started simulating by first modeling the transmitter and receiver coils in Solidworks software (outlined in red in Fig. 1A). The transmitter was modeled with 18 circular turns of a 23 AWG wire with spacing equivalent to the wire diameter, resulting in an inner diameter of 10 mm and outer diameter of 40 mm. The receiver was modeled with 5 circular turns of a 30 AWG wire connected to a meandering tail, all of which was folded into a half-cylindrical shape with a diameter of 2.8 mm and length of 15 mm. Next, we imported the components into ANSYS Maxwell simulation software and positioned them at an initial mean distance of 20 mm apart [44]. The position and angle of the receiver in each frame was adjusted based on computed centroid position and normal vector of the phantom from the MRI tracings. Using the Eddy Current solver in ANSYS Maxwell, we simulated the magnetic (B) field resulting from the 13.56 MHz alternating current in the transmitting coil and its impact on the receiving coil. The coils' internal resistance and inductance as well as the coupling coefficient between the interacting components were computed by the solver and imported into PSPICE Electronic Circuit Optimization & Simulation software. We simulated the circuit of Fig. 1A with a 1000 Ω load [45]. We measured the voltage across the load in the receiver given an instantaneous input power of 1.26 W to the transmitter.

Finally, we computed SAR using the simulated E-Field in ANSYS Maxwell FEM software as needed for Equation (7):

$$SAR = \frac{\sigma E^2}{\rho} \quad (7)$$

where σ is the electrical conductivity of the tissue and ρ is the mass density of the tissue.

III. RESULTS

A. Measurement of Wireless Power Transfer Range

To determine the range of power transfer for the proposed pacer, we placed the transmitter and receiver at various distances apart with different degrees of misalignment (Fig. 4A). Output voltage was compared against the mean pacing amplitude of 0.80 V [34] (dotted line

at the upper boundary of the red zones in Fig. 4B–F) and maximum potential amplitude of the market-released leadless pacemaker at 5 V [6] (dotted line at the upper boundary of the green zones in Fig. 4B–F). To evaluate the potential safety margin for the proposed system, we defined four conservative conditions for testing the wireless pacer:

- (1) With pacing durations typically established between 0.2 ms to 1 ms, we elected a 1 ms pulse duration to examine the maximum total power consumption. This power consumption can be reduced up to 80% with a shorter pulse duration (< 1 ms).
- (2) In the setting of short intermittent pulse delivery, Specific Absorption Rate (SAR) can be reduced to significantly below the limits set by the Federal Communications Committee (FCC) [47]. We performed our studies using 1.26 W of instantaneous power, equivalent to a low average input power of 1.26 mW as a result of the 1 ms pulse width. The pacer has the potential for a higher voltage amplitude at the stimulating electrodes by increasing this input power.
- (3) Cardiothoracic Magnetic Resonance Images (MRI) have demonstrated a mean distance of 20 mm between the location of the subcutaneous transmitter (Tx) in the anterior chest, and the location of the pacer (Rx) in the ACV [44]. The distance between the Tx and Rx was examined at 10 mm greater than the mean anatomical displacement to assess safety margins. As power transfer efficiency (PTE) decreases exponentially over distance, a 30 mm Tx-to-Rx separation demonstrates the extent of the positional safety margin with the given parameters.
- (4) To demonstrate the effect of cardiac motion, we simulated Tx-to-Rx misalignment at up to two-fold the angular change measured throughout a cardiac cycle in our MRI-Phantom studies. This wide-range analysis allowed for the assessment of the angular safety margin available in the designed pacer.

At 20 mm mean displacement and up to 20° misalignment, the intravascular pacer consistently achieved a pacing amplitude > 5 V (Fig. 4). The amplitude remained above the mean pacing threshold of 0.80 V in nearly all combinations of displacement and misalignment. At a displacement of 30 mm (10 mm above the mean), the pacing amplitude remained more than twice the mean amplitude of 0.80 V in all cases except for horizontal misalignments $> 20^\circ$.

Also notable is the non-linear relationship between vertical misalignment and voltage amplitude, where power transfer efficiency increases with some degrees of misalignment. This angular adaption is an important characteristic of the designed receiver coil of the pacer unit. The bending of the circular planar loop into the z-axis generates a diagonal capture of the magnetic field; thus, negating the power losses from changes in angular misalignment (Fig. 4G–H). This advantage supplements the antenna's hollow cylindrical shape to allow for blood flow through the cylindrical pacer unit.

B. Simulating Pacing Function Across a Cardiac Cycle

A phantom pacer was integrated into thoracic MRIs at the position of the ACV and tracked throughout a cardiac cycle to determine the relative motion (position and angle) between the subcutaneous transmitter and pacer unit (left inset of Fig. 5A–i–ix). In addition, the magnetic

field (B) generated from the alternating current (AC) excitation in the transmitter coil was determined over nine time points in the cardiac cycle (right inset of Fig. 5A–i–ix). Inductive power transfer (IPT) simulations at the end of systole (Fig. 5A–i) and diastole (Fig. 5A–iv) demonstrated sufficient power transfer at the two spectra of the cardiac cycle. The change in pacer position compared to the initial time frame, which remained below 6 mm and 20° of misalignment, and the resulting B-field interaction between the pacer and its transmitter (enhanced in zoomed-in view in Fig. 5A–x) revealed the effect of cardiac contraction-mediated transmitter-receiver interaction. The maximum difference in field potential was observed when the pacer was in the red region of the B-field ($B = 0.0001$ T) (Fig. 5A–vi), as compared to the green region ($B = 0.00005$ T) (Fig. 5A–i).

The outcome of the B-field strength was demonstrated in terms of the change in power transfer efficiency (PTE) (Fig. 5B). PTE directly affects the output voltage, which remained above the peak voltage capacity of 5V throughout the recorded cycle (Fig. 5C). The capacity to deliver short intermittent pulses allowed us to maintain this threshold with low power consumption and tissue absorption despite the low PTE ranging from 2.7% to 7.6%.

Notably, SAR remained significantly below the FCC safety limits. The electric (E) field strength at peak coupling (Fig. 5D) was computed to determine maximum tissue absorption. Based on peak E-field strength (Fig. 5D), conductivity values, and density values (Fig. 5E), maximum absorption at 1.26 mW of input power was computed as 0.07 W kg. This is nearly 23 times less than the FCC safety limit of 1.6 W kg [47]. For this reason, the simulations established a basis for complying with the SAR safety standards while maintaining the capacity to increase input power to the intravascular pacer in the setting of anatomical variations that deviate significantly from the mean MRI-based measurements.

Similar to the bench experiments, small vertical misalignments engendered an increase in the power transfer efficiency and output voltage (Fig. 5B–C). Also, although pacing occurs only once per cycle, our simulation experiments established the fundamental capacity to maintain sufficient power transmission throughout the cardiac cycle.

IV. DISCUSSION

For decades, implantable electronics have paved the way for life-changing therapies, including artificial pacing for cardiac rhythm disorders and neural stimulation for movement disorders, gastric immobility, and bladder contraction. However, a fundamental design challenge for implantable devices is the power source and its inherent impact on device size. We hereby demonstrated a batteryless and wireless pacer that enables catheter-based intravascular deployment. In essence, the presented architecture works substantially similar to existing lead-based pacemakers with the exception of having a physical connection between the pulse generator and the pacing electrodes. While these “remote-controlled electrodes” are more power-consumptive than a wired system, they have the capacity to significantly decrease patient morbidity and mortality associated with lead-based devices. We reduced the impact on power consumption using the presented intermittent transmission control architecture. The 3 mm diameter wireless pacer was sufficiently powered for continuous pacing using 1.26 mW of power from a 40 mm diameter transmitter while

remaining nearly 23 times below the SAR safety limits. This power requirement may be fulfilled via a rechargeable battery with charging intervals of over 5 months or up to years, depending on the pacing demand [48].

The control architecture of a wirelessly powered system is fundamental to its application in implantable devices. The control circuitry of most inductive power transfer systems is positioned within the stimulating unit, thus requiring continuous power delivery [16]–[30]. Two approaches have been sought to address this architecture: (1) direct wireless power transfer or (2) battery-based power delivery. The former entails direct wireless power transfer to be sufficiently high to satisfy both the internal control circuit and tissue stimulation. Therefore, this system requires significant power delivery in the setting of weak coupling between the transmitter and a small-scale receiver, resulting in tissue heating over multi-centimeter ranges. The latter addresses the limitations of direct wireless power at the expense of an integrated battery and, consequently, device size. Thus, currently available inductive power transfer systems demand sacrifice in either size or efficiency.

In our intravascular pacer, we embedded the control circuitry for pulse modulation within the transmitter; thus, the solution to size and inefficiency were not forced into mutual exclusivity. Using the transmitter as the primary controller, we compartmentalized the function of the receiver to only a transformation unit that is activated solely during the short period of stimulation. Hence, eliminating the battery mitigated the size issue, and transmitting intermittent wireless pulses compensated for power transfer inefficiency.

Notably, intermittent power delivery allowed for reduced receiver size by tolerating a more weakly-coupled system while supplying sufficient power for stimulation. The tolerance for amplifying wireless power transmission is prominently constrained by SAR limits, which is in turn dependent on the duration of power transfer. Thus, instantaneous power delivery could be amplified by providing short-length pulses rather than continuous transmissions. The coupling coefficient (k) is impacted by the distance between the interacting coils and their geometry as defined by Equation (2). A system that tolerates weak coupling thus allows for a small receiver coil (d_2) with a large distance (D) between the transmitter and receiver, rendering our control architecture optimal for biomedical implants which face anatomical constraints and variations. In this context, the anatomic constraint of a coronary vein in the anterior cardiac wall warranted a receiver coil design with < 3 mm diameter. As elucidated in our simulation and bench experiments, the resulting power transfer efficiency was measured to be below 10% in response to a combination of displacements and misalignments. Nonetheless, sufficient power for pacing was established while remaining below the SAR limits. This outcome enables further increases in power delivery from the transmitter in the potential setting of additional anatomical constraints and motion. Furthermore, while epicardial pacing has been previously demonstrated to have similar thresholds as endocardial pacing [49]–[51], the flexibility for increased power transmission can compensate for any potential variations in pacing conduction and total activation time in epicardial pacing.

Finally, while the current pacer form-factor utilizes inflexible coils, future work will establish the fabrication of a flexible device to allow for intravascular delivery distal to the

coronary sinus with the capacity to navigate the tortuous vasculature. This flexible device can be made possible by employing a biocompatible parylene-C substrate for printed coils and by scaling down the supporting circuitry using integrate chip (IC) technology [52], [53].

V. CONCLUSION

This work presents the groundwork for extensive device miniaturization using a unique control system architecture and coil design with the capacity for low power consumption in the setting of inherent efficiency and absorption limitations. This can be valuable for the practical utilization of inductive power transfer in the application of medical devices, in which anatomical constraints hinder operational capacity. While there remain challenges with regards to flexible device microfabrication and intravascular delivery strategy, the fundamental work here provides a basis for encouraging outcomes. Our successful studies thus inspire a promise for a wireless stimulator with an intravascular deployment strategy, with translational indications for eliminating complications associated with device leads, repeated surgeries for battery replacement, and mechanically-burdened fixation failure points.

Acknowledgments

This work was supported by National Institute of Health HL118650 (TKH), HL129727 (TKH), HL111437 (TKH), BX004356 (TKH), EB0220002 (TKH), and NIH NIGMS training grant GM008042 (PA) and UCLA David Geffen Scholarship (PA).

VI. REFERENCES

- [1]. Mond HG and Proclemer A, "The 11th world survey of cardiac pacing and implantable cardioverter-defibrillators: Calendar year 2009 - A world society of Arrhythmia's project," *PACE - Pacing Clin. Electrophysiol.*, vol. 34, no. 8, pp. 1013–1027, 2011. [PubMed: 21707667]
- [2]. Kirkfeldt RE, Johansen JB, Nohr EA, Jorgensen OD, and Nielsen JC, "Complications after cardiac implantable electronic device implantations: An analysis of a complete, nationwide cohort in Denmark," *Eur. Heart J.*, vol. 35, no. 18, pp. 1186–1194, 2014. [PubMed: 24347317]
- [3]. Hauser RG, Katsiyannis WT, Gornick CC, Almquist AK, and Kallinen LM, "Deaths and cardiovascular injuries due to device-assisted implantable cardioverter-defibrillator and pacemaker lead extraction," *Europace*, vol. 12, no. 3, pp. 395–401, 2010. [PubMed: 19946113]
- [4]. Sperzel J et al., "State of the art of leadless pacing," *Europace*, vol. 17, no. 10, pp. 1508–1513, 2015. [PubMed: 26024918]
- [5]. "FDA Executive Summary Memorandum General Issues: Leadless Pacemaker Devices," Gaithersburg, 2016.
- [6]. "Micra TM MC1VR01 Clinical Manual," Minneapolis, 2016.
- [7]. Hwang GT et al., "Self-powered cardiac pacemaker enabled by flexible single crystalline PMN-PT piezoelectric energy harvester," *Adv. Mater.*, vol. 26, no. 28, pp. 4880–4887, 2014. [PubMed: 24740465]
- [8]. Karami MA and Inman DJ, "Powering pacemakers from heartbeat vibrations using linear and nonlinear energy harvesters," *Appl. Phys. Lett.*, vol. 100, no. 4, 2012.
- [9]. Glynne-Jones P, Beeby SP, and White NM, "Towards a piezoelectric vibration-powered microgenerator," *IEE Proc. - Sci. Meas. Technol.*, vol. 148, no. 2, p. 68, 2001.
- [10]. Tashiro R, Kabei N, Katayama K, Tsuboi F, and Tsuchiya K, "Development of an electrostatic generator for a cardiac pacemaker that harnesses the ventricular wall motion," *J. Artif. Organs*, vol. 5, no. 4, pp. 239–245, 2002.

- [11]. Auricchio A, Delnoy PP, Regoli F, Seifert M, Markou T, and Butter C, "First-in-man implantation of leadless ultrasound-based cardiac stimulation pacing system: Novel endocardial left ventricular resynchronization therapy in heart failure patients," *Europace*, vol. 15, no. 8, pp. 1191–1197, 2013. [PubMed: 23703364]
- [12]. Lee KL, "In the wireless era: leadless pacing.," *Expert Rev. Cardiovasc. Ther.*, vol. 8, no. 2, pp. 171–174, 2010. [PubMed: 20136603]
- [13]. Ozeri S, Shmilovitz D, Singer S, and Wang CC, "Ultrasonic transcutaneous energy transfer using a continuous wave 650 kHz Gaussian shaded transmitter," *Ultrasonics*, vol. 50, no. 7, pp. 666–674, 2010. [PubMed: 20219226]
- [14]. Ozeri S and Shmilovitz D, "Ultrasonic transcutaneous energy transfer for powering implanted devices," *Ultrasonics*, vol. 50, no. 6, pp. 556–566, 2010. [PubMed: 20031183]
- [15]. Ouyang H et al., "Symbiotic cardiac pacemaker," *Nat. Commun.*, vol. 10, no. 1, 2019.
- [16]. Laughner JI et al., "A Fully Implantable Pacemaker for the Mouse: From Battery to Wireless Power," *PLoS One*, vol. 8, no. 10, pp. 1–8, 2013.
- [17]. Ali H, Ahmad TJ, and Khan SA, "Inductive Link Design for Medical Implants," in *IEEE Symposium on Industrial Electronics and Applications*, 2009, pp. 694–699.
- [18]. Kurs A, Karalis A, Moffatt R, Joannopoulos JD, Fisher P, and Soljacic M, "Wireless power transfer via strongly coupled magnetic resonances.," *Science*, vol. 317, no. 5834, pp. 83–86, 2007. [PubMed: 17556549]
- [19]. RamRakhyani AK, Mirabbasi S, and Chiao M, "Design and optimization of resonance-based efficient wireless power delivery systems for biomedical implants," *IEEE Trans. Biomed. Circuits Syst.*, vol. 5, no. 1, pp. 48–63, 2011. [PubMed: 23850978]
- [20]. Kiani M, Jow UM, and Ghovanloo M, "Design and Optimization of a 3 Coil Inductive Link for Efficient Wireless Power Transmission," *IEEE Trans. Biomed. Circuits Syst.*, vol. 5, no. 6, pp. 579–591, 2011.
- [21]. Lee SY et al., "A programmable implantable microstimulator soc with wireless telemetry: Application in closed-loop endocardial stimulation for cardiac pacemaker," in *IEEE Transactions on Biomedical Circuits and Systems*, 2011, vol. 5, no. 6, pp. 511–522. [PubMed: 23852549]
- [22]. Cruciani S, Campi T, Maradei F, and Feliziani M, "Numerical simulation of Wireless Power Transfer system to recharge the battery of an implanted cardiac pacemaker," in *IEEE International Symposium on Electromagnetic Compatibility*, 2014, pp. 44–47.
- [23]. Li X, Tsui CY, and Ki WH, "A 13.56 MHz Wireless Power Transfer System With Reconfigurable Resonant Regulating Rectifier and Wireless Power Control for Implantable Medical Devices," *IEEE J. Solid-State Circuits*, vol. 50, no. 4, pp. 978–989, 2015.
- [24]. Jow U and Ghovanloo M, "Design and Optimization of Printed Spiral Coils for Efficient Transcutaneous Inductive Power Transmission," *Optimization*, vol. 1, no. 3, pp. 193–202, 2008.
- [25]. Loeb GE, Zamin CJ, Schulman JH, and Troyk PR, "Injectable microstimulator for functional electrical stimulation," *Med. Biol. Eng. Comput.*, 1991.
- [26]. Loeb GE et al., "Design and testing of a percutaneously implantable fetal pacemaker," *Ann. Biomed. Eng.*, 2013.
- [27]. Vest AN et al., "Design and Testing of a Transcutaneous RF Recharging System for a Fetal Micropacemaker," *IEEE Trans. Biomed. Circuits Syst.*, 2017.
- [28]. Bar-Cohen Y et al., "Minimally Invasive Implantation of a Micropacemaker into the Pericardial Space," *Circ. Arrhythmia Electrophysiol.*, 2018.
- [29]. Heetderks WJ, "RF Powering of Millimeter- and Submillimeter-Sized Neural Prosthetic Implants," *IEEE Trans. Biomed. Eng.*, vol. 35, no. 5, pp. 323–327, 1988. [PubMed: 3397079]
- [30]. Von Arx JA and Najafi K, "A wireless single-chip telemetry-powered neural stimulation system," 1999 *IEEE Int. Solid-State Circuits Conf. Dig. Tech. Pap. ISSCC. First Ed. (Cat. No.99CH36278)*, no. June 1995, pp. 214–215, 1999.
- [31]. Bakogianni S and Koulouridis S, "Sub-1 GHz far-field powering of implantable medical devices: Design and safety considerations," in *IEEE Antennas and Propagation Society, AP-S International Symposium (Digest)*, 2015, vol. 2015-October, pp. 942–943.

- [32]. Liu C, Guo YX, Sun H, and Xiao S, "Design and safety considerations of an implantable rectenna for far-field wireless power transfer," *IEEE Trans. Antennas Propag*, vol. 62, no. 11, pp. 5798–5806, 2014.
- [33]. Sun Y, Greet B, Burkland D, John M, Razavi M, and Babakhani A, "Wirelessly powered implantable pacemaker with on-chip antenna," in *IEEE MTT-S International Microwave Symposium Digest*, 2017, pp. 1242–1244.
- [34]. Kristiansen H, Hovstad T, Vollan G, and Faerestrands S, "Right ventricular pacing and sensing function in high posterior septal and apical lead placement in cardiac resynchronization therapy," *Indian Pacing Electrophysiol. J*, vol. 12, no. 1, pp. 4–14, 2012. [PubMed: 22368376]
- [35]. Astrinsky E and Furman S, "Pacemaker Output Programming for Maximum Safety and Maximum Longevity," *J. Cardiovasc. Electrophysiol*, vol. 1, no. 1, pp. 51–58, 1983.
- [36]. Kiani M and Ghovanloo M, "A figure-of-merit for designing high-performance inductive power transmission links," *IEEE Trans. Ind. Electron*, vol. 60, no. 11, pp. 5292–5305, 2013.
- [37]. Finkenzeller K, *RFID Handbook: Fundamentals and Applications in Contactless Smart Cards, Radio Frequency Identification and near-Field Communication*, Third. Chippingham, Wiltshire, UK: John Wiley & Sons, 2010.
- [38]. Chen SCQ and Thomas V, "Optimization of Inductive RFID Technology," *Int. Symp. Electron. Environ*, no. 2, pp. 82–87, 2001.
- [39]. Nan Xi and Sullivan CR, "An improved calculation of proximity-effect loss in high-frequency windings of round conductors," in *IEEE 34th Annual Conference on Power Electronics Specialist*, 2003, pp. 853–860.
- [40]. Sokal NO, "Class-E RF Power Amplifiers," *QEX Commun. Quart*, vol. 204, pp. 9–20, 2001.
- [41]. Senjuti S, "Design and Optimization of Efficient Wireless Power Transfer Links for Implantable Biotelemetry Systems," *THESIS - U West. Ontario_UWO*, 2013.
- [42]. Terman F, "Radio engineer's handbook," *Text. Res. J*, 1943.
- [43]. Sun JP, Yang XS, Lam YY, Garcia MJ, and Yu CM, "Evaluation of Coronary Venous Anatomy by Multislice Computed Tomography," *World J. Cardiovasc. Surg*, vol. 2, no. 4, pp. 91–95, 2012.
- [44]. Abiri P et al., "Inductively powered wireless pacing via a miniature pacemaker and remote stimulation control system," *Sci. Rep*, vol. 7, no. 1, 2017.
- [45]. Berger T, Roithinger FX, Antretter H, Hangler H, Pachinger O, and Hintringer F, "The Influence of High Versus Normal Impedance Ventricular Leads on Pacemaker Generator Longevity," *PACE - Pacing Clin. Electrophysiol*, vol. 26, no. 11, pp. 2116–2120, 2003. [PubMed: 14622313]
- [46]. Abiri A et al., "Simulating Developmental Cardiac Morphology in Virtual Reality Using a Deformable Image Registration Approach," *Ann. Biomed. Eng*, vol. 46, no. 369, pp. 1–12, 2018. [PubMed: 29019076]
- [47]. Cleveland RF, Sylvar DM, and Ulcek JL, "Evaluating Compliance with FCC Guidelines for Human Exposure to Radiofrequency Electromagnetic Fields," Washington, D.C., 1997.
- [48]. Abiri P et al., "Wireless Pacing Using an Asynchronous Three-Tiered Inductive Power Transfer System," *Ann. Biomed. Eng*, 2020.
- [49]. Dhar SK, Heston KJ, Madrak LJ, Shah BK, Deger FT, and Greenberg RM, "Strength duration curve for left ventricular epicardial stimulation in patients undergoing cardiac resynchronization therapy," *PACE - Pacing Clin. Electrophysiol*, 2009.
- [50]. Sachweh JS et al., "Twenty years experience with pediatric pacing: Epicardial and transvenous stimulation," *Eur. J. Cardio-thoracic Surg*, 2000.
- [51]. Beaufort-Krol GCM, Mulder H, Nagelkerke D, Waterbolk TW, and Bink- Boelkens MTE, "Comparison of longevity, pacing, and sensing characteristics of steroid- eluting epicardial versus conventional endocardial pacing leads in children," *J. Thorac. Cardiovasc. Surg*, 1999.
- [52]. Chen PJ, Saati S, Varma R, Humayun MS, and Tai YC, "Implantable flexible-coiled wireless intraocular pressure sensor," in *Proceedings of the IEEE International Conference on Micro Electro Mechanical Systems (MEMS)*, 2009.
- [53]. Wanlass FM, "Low Stand-By Power Complementary Field Effect Circuitry," *US Pat. 3,356,858*, 1967.

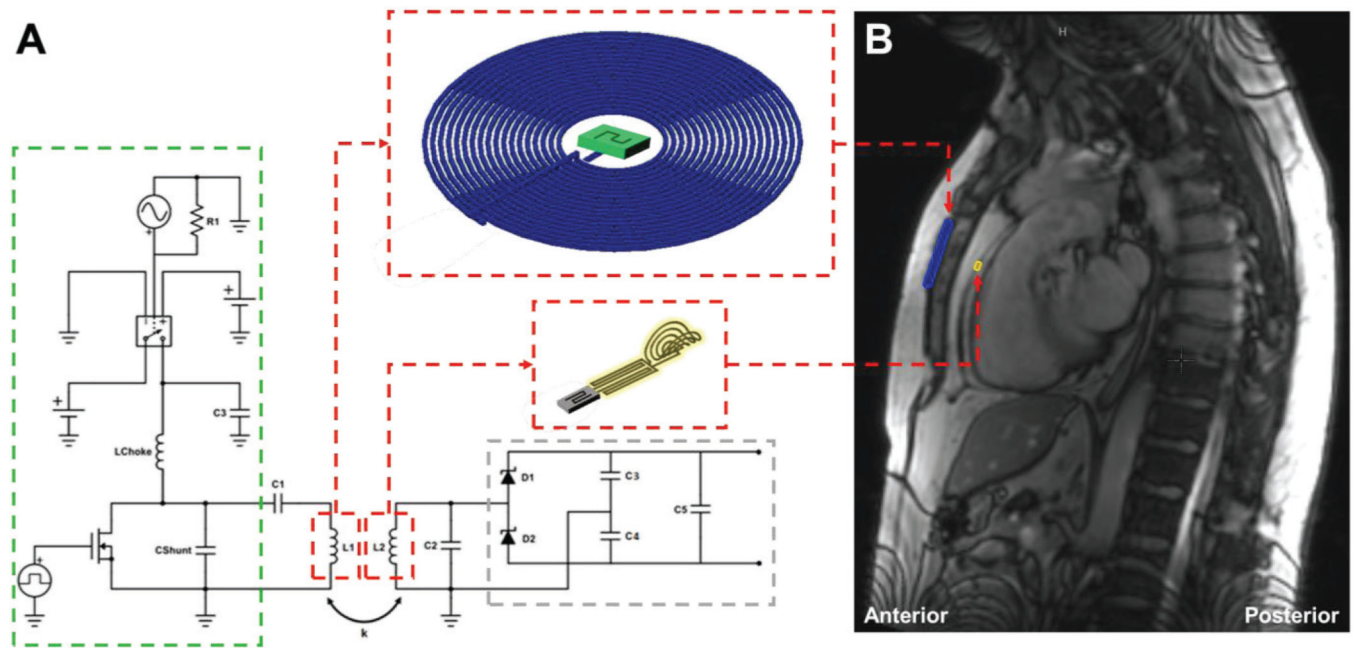


Fig. 1: Circuit and Coil Design

(A) Transmitter and receiver circuit design. Highlighted in the green is the control circuitry that determines pacing rate, rhythm, and level of power input. Highlighted in grey is the receiver circuitry for power conversion. Highlighted in red are the transmitter and receiver coils as positioned in the circuit as well as their structure. (B) Anatomical position of the subcutaneous transmitter in blue and intravascular receiver in yellow, depicted on a sagittal section of a human MRI.

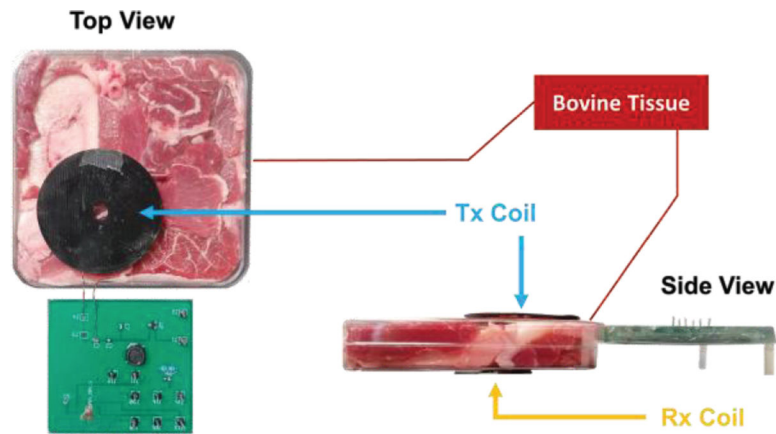


Fig. 2: In Vitro Experimental Setup.

Photo of experimental setup for in vitro analysis of power transfer efficiency over various distances and misalignment levels. A segment of bovine tissue containing a mixture of muscle, adipose, and bone was placed in between the two coils to mimic the environment of the body.

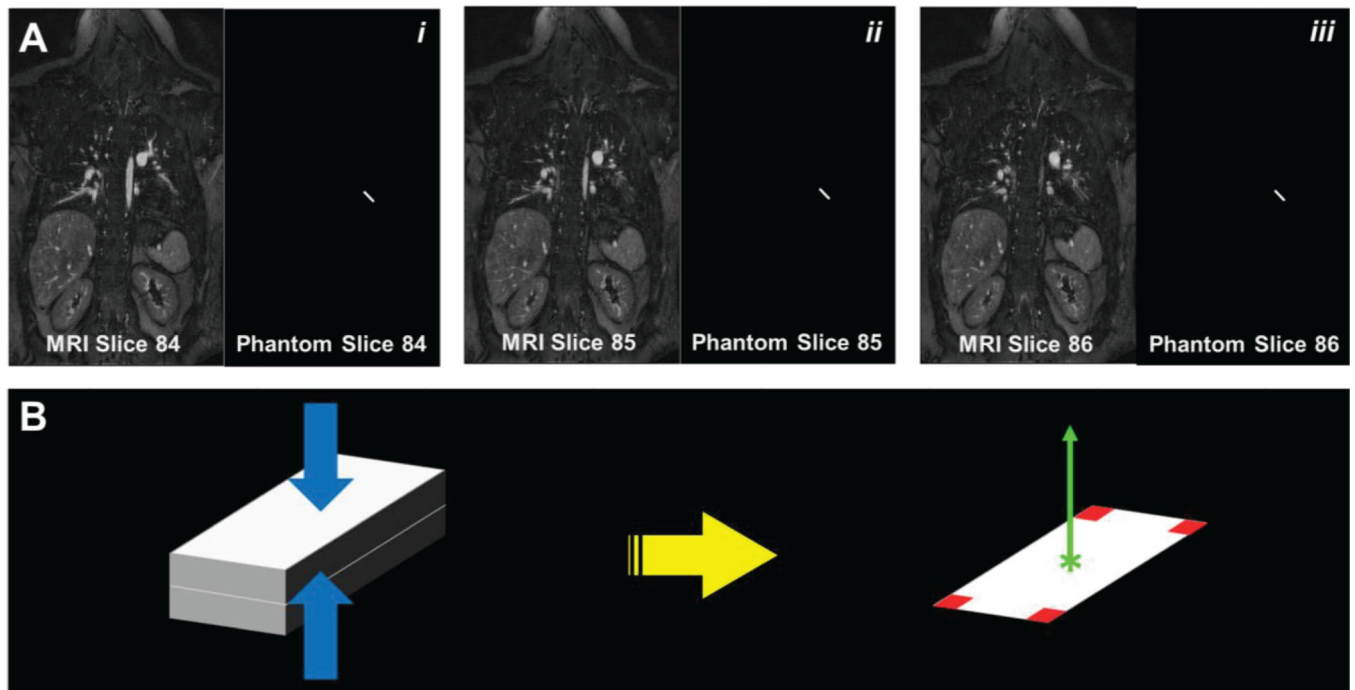


Fig. 3: MRI-Phantom Study Data Processing.

(A) Coronal MRI slices and corresponding “pacer” phantom placements across the three representative slices; (B) The location of the red landmarks was calculated by taking the average of their position to create a 2-D version of the object. The centroid and normal vector were then computed based on the averaged red marks that represented the four corners.

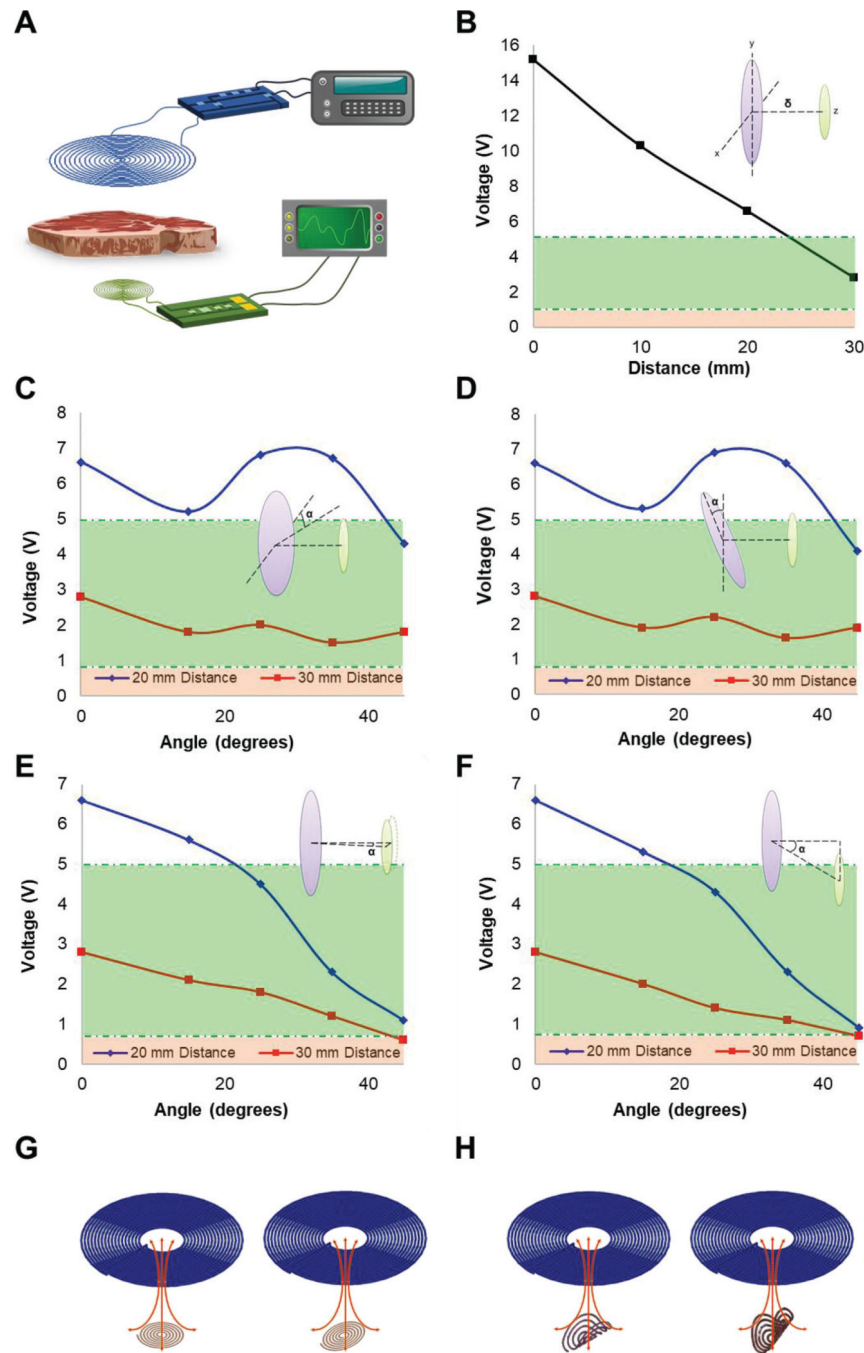


Fig. 4: In Vitro Experiments.

(A) A schematic of the experimental configuration illustrates the transmitter and receiver position across a segment of bovine tissue. (B) Output voltage decreased as the displacement between the transmitter and receiver, δ , increased from 0 to 30 mm at $\delta = 20$ mm and $\delta = 30$ mm. (C) Output voltage fluctuated in response to x-axis vertical misalignment, α , ranging from 0 to 45 degrees at $\delta = 20$ mm and $\delta = 30$ mm. (D) Output voltage fluctuated in response to y-axis vertical misalignment, α , ranging from 0 to 45 degrees at $\delta = 20$ mm and $\delta = 30$ mm. (E) Output voltage decreased in response to x-axis horizontal misalignment, α ,

ranging from 0 to 45 degrees at $\delta = 20$ mm and $\delta = 30$ mm. (F) Output voltage decreased in response to y-axis horizontal misalignment, α , ranging from 0 to 45 degrees at $\delta = 20$ mm and $\delta = 30$ mm. (G) The effect of B-field (red arrows) capture is shown with a planar circular receiver coil in the presence of absence of misalignment. (H) The effect of B-field (red arrows) capture is shown with a half-cylindrical receiver coil in the presence of absence of misalignment. (B-F) Output voltage was compared against the average pacing amplitude of 0.80 V (dotted line at the upper boundary of the red zones) and maximum potential pacing amplitude of the market-released leadless pacemaker at 5 V (dotted line at the upper boundary of the green zones).

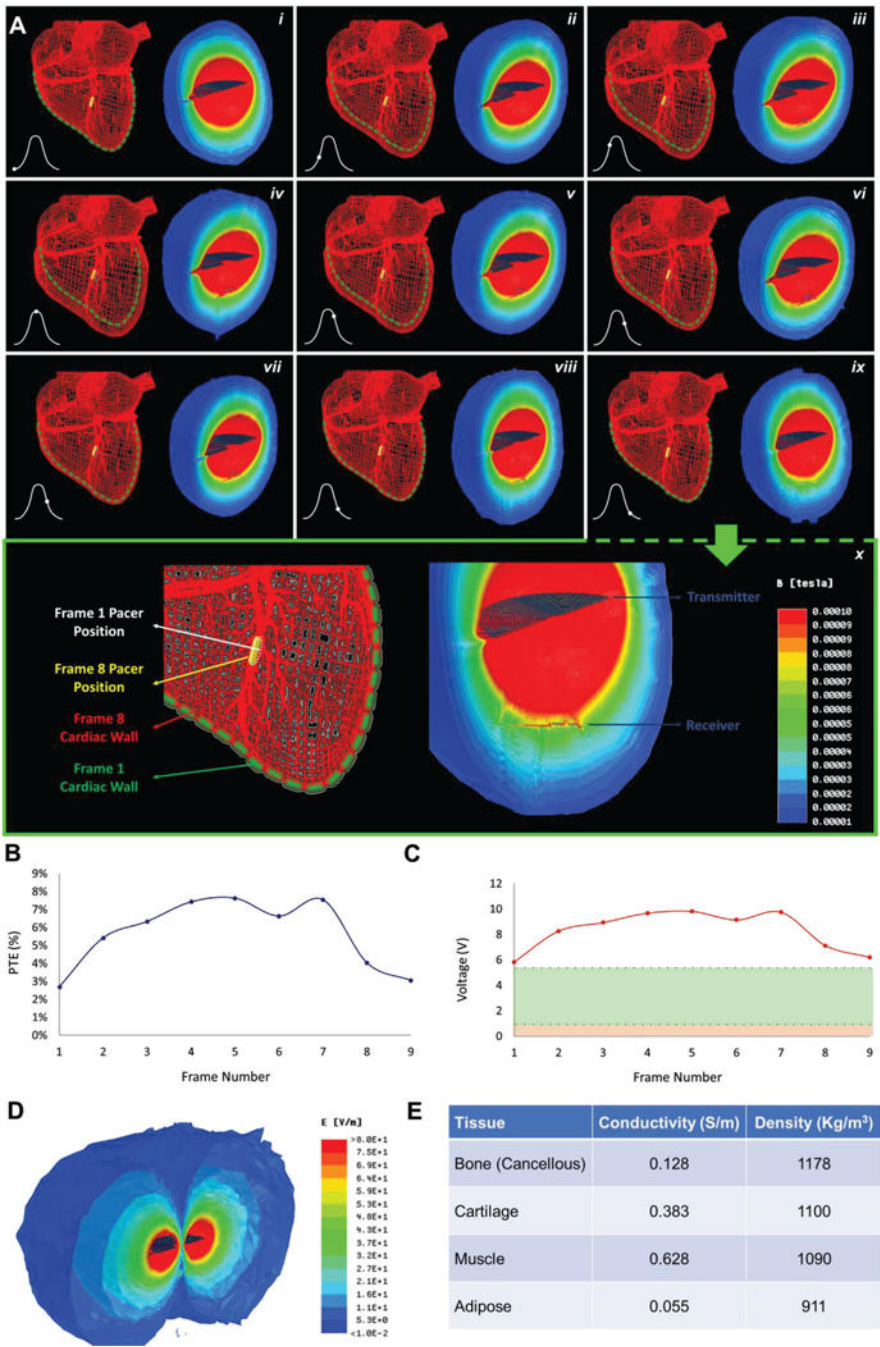


Fig. 5: Cardiac Cycle Simulation Experiments.

(A) Each box represents one timeframe in the cardiac cycle in (i)-(ix). Cardiac contraction and consequential pacer positional and angular motion are shown in the schematic on the left inset. Stimulation of the interaction between the transmitter and receiver coil is demonstrated by the magnetic field shown on the right inset. (x) demonstrates a zoomed-in view of the events in box (ix). (B) Computed power transfer efficiency (PTE) over the nine captured frames of the cardiac cycle. (C) Computed maximum potential voltage threshold over the nine captured frames of the cardiac cycle given an average input power of 1.26 mW.

(D) Electric field simulation of Frame 5 of the cardiac cycle at which time point maximum coupling was observed. (E) Various tissue conductivities and densities, which, in combination with the Electric field, determine SAR.

TABLE I**TRANSMITTER & RECEIVER COIL DESIGN**

Coil	Inductance	Capacitance
Receiver	130 nH	1050 pF
Transmitter	7.15 uH	19.3 pF

Author Manuscript

Author Manuscript

Author Manuscript

Author Manuscript